

Universality in quantum critical flow of charge and heat in ultraclean graphene

In the format provided by the
authors and unedited

Contents

Page No.

S1. The experimental strategy	2
S2. Characterisation of cleanliness of our hBN-encapsulated graphene devices	3
S3. Calculation of the diffusive mean free path in our devices	5
S4. Thermal transport measurement	6
S5. Equations for electron hydrodynamics	8
S6. Electrical conductivity of hydrodynamic electrons	10
S7. Violation of Wiedemann-Franz Law in lower mobility devices	12
S8. Quantum critical conductivity for hydrodynamic electrons	15
S9. Relation between the shear viscosity and enthalpy density	16
S10. Thermal modelling of the hBN-encapsulated graphene devices	17

S1. The experimental strategy:

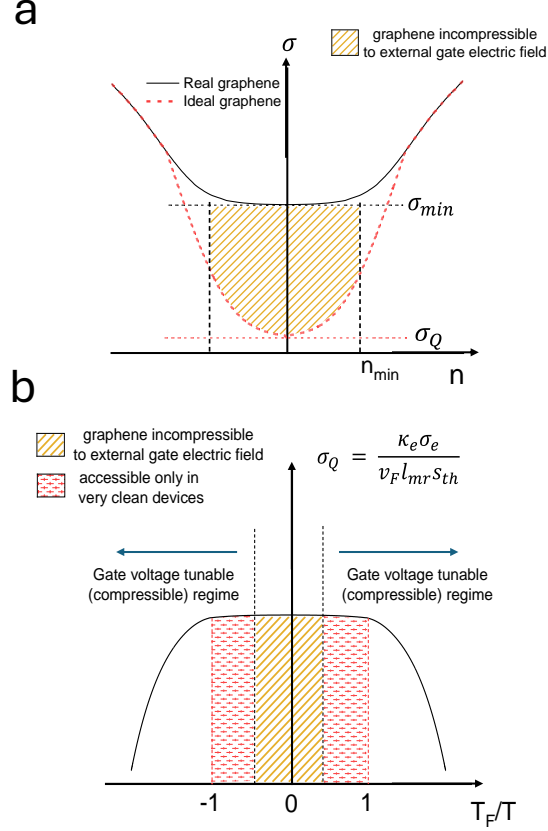


Figure S1. **Carrier density dependence of electrical and thermal conductivity in practical graphene devices:** (a) The red-coloured curve represents an ideal graphene in which electrical conductivity near the quantum critical Dirac point approaches universal conductivity σ_Q . The black-coloured curve represents a realistic graphene device. The presence of a finite amount of charge inhomogeneity n_{min} (depicted by the vertical black dashed lines) causes σ to saturate to σ_{min} (depicted by a horizontal black dashed line) for $n \leq n_{min}$ and hence, σ_Q falls inside an experimentally inaccessible region (denoted by yellow stripes). (b) Our experimental strategy relies on analysing the behaviour of the quantity $\kappa_e \sigma_e / v_F l_{mr} s_{th}$ as a function of T_F/T , which is denoted by the black curve. The yellow striped region, where $T_F/T = T_F^0/T < 1$ where $T_F^0 = \hbar v_F \sqrt{\pi n_{min}} / k_B$ remains experimentally inaccessible, but the red striped region ($T_F^0 \leq T_F \leq T$) becomes accessible in ultra-clean devices for the evaluation of σ_Q .

S2. Characterisation of cleanliness of the hBN-encapsulated graphene devices:

Experimental realisation of electron hydrodynamics in a solid-state system requires a very high degree of cleanliness because disorders and impurities tend to relax the electron momentum, suppressing the fluidic nature of electron transport. Previous experimental efforts to explore electron hydrodynamics have also suffered largely due to this reason. Over the past decade, graphene has emerged as a viable candidate where one can achieve a significantly high degree of cleanliness. Even then, recent experiments had to mainly resort to constriction-based and Corbino geometries, in the absence of disorder-free fabrication procedures. In this scenario, in order to reach “ultra-clean”, we have adopted the following strategies:

1. **Surface topography scans of the hBN flakes:** Hexagonal boron nitride is considered to be an ideal substrate for graphene-based 2D transistors [1]. However, reports [2] have confirmed the presence of inhomogeneity and tape residue on the surface of thick hBN flakes (> 5 nm), originating during exfoliation, which can give rise to defect states, acting as traps during electrical transport. These surface contaminants are usually distributed non-uniformly over the flake and can be easily detected by scanning the topography using atomic force microscopy (AFM). The hBN flakes chosen for device fabrication (Fig. S2a, for example) were scanned for regions with minimal surface inhomogeneity as shown in Figs. S2b and S2c. The highlighted portion of the AFM line scans in Fig. S2c has a surface roughness of (0.2 ± 0.07) nm. These “flat” portions of the hBN flakes are homogeneous and clean, and have been selectively used for placing the graphene layer on top.
2. **Spectroscopic investigation of defects in graphene:** In case of graphene, the layer number and spatial distribution of defects can be easily identified using Raman spectroscopy [3]. One such spectrum is depicted in Fig. S2d, for the graphene flake shown in Inset. The G and 2D peaks are clearly visible at wavenumbers 1581 cm^{-1} and 2689 cm^{-1} respectively (Fig. S2e), which indicate a very low degree of intrinsic charge inhomogeneity in graphene [4]. Further, the Full Width at Half-Maximum (FWHM) of the G and 2D peaks (15 cm^{-1} and 26 cm^{-1} respectively, (Fig. S2e)) indicates a weak electron-phonon coupling, as expected in pristine monolayer graphene [5]. Also,

the absence of the D Raman peak and a low signal-to-noise ratio are considered to be crucial evidence for a clean monolayer graphene [4].

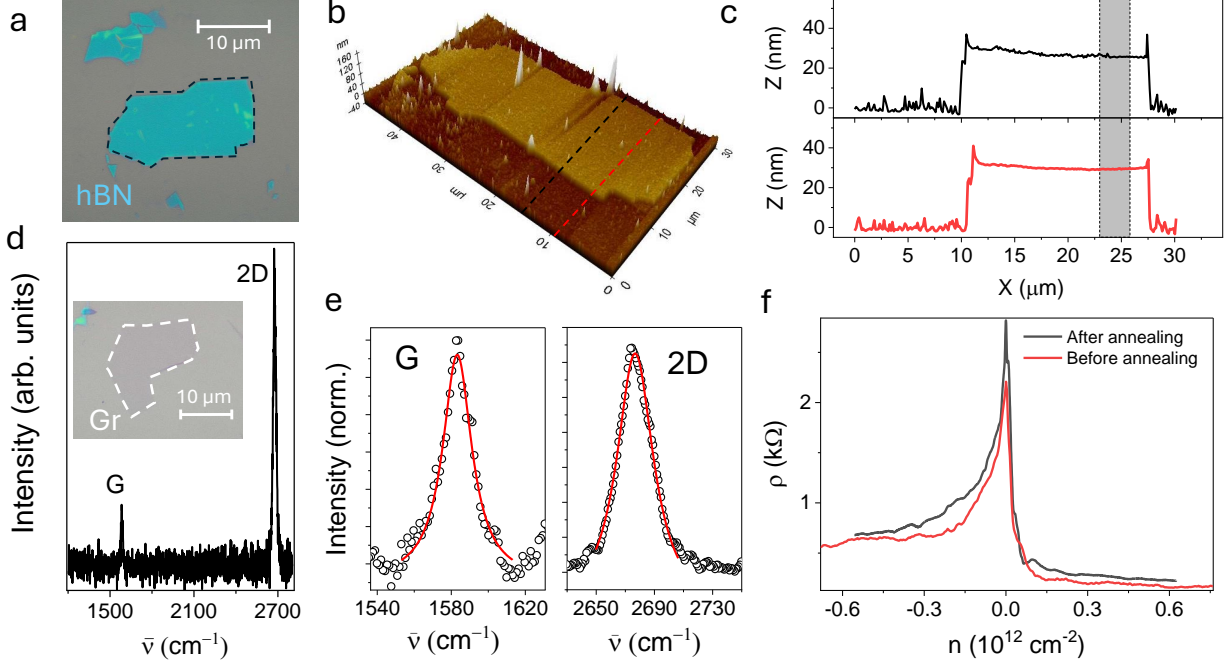


Figure S2. **Cleaning procedures adopted during fabrication:** (a) Optical micrograph of an exfoliated hBN flake. (b) 3D AFM imaging of the hBN flake. (c) Height profile of the hBN flake at two different line cuts, indicated by red and black dashed lines in (b). The highlighted portion of the line scans has a surface roughness of $\simeq 0.2$ nm. (d) Raman spectrum of a pristine monolayer graphene flake shown in Inset. (e) Lorentzian fitting of the G and 2D Raman peaks to calculate the exact position of the two peaks, along with their respective linewidths. (f) Transfer characteristics of device D1S2 before and after low-temperature current annealing.

3. Viscoelastic dry transfer method using a van der Waals pick up layer: Once clean flakes have been procured, and their cleanliness has been verified, the next key step is the systematic transfer of the layers into a stack without introducing any additional impurities, organic residues or surface contaminants in the process. Dry transfer techniques are well known for introducing minimal contamination in the “pick-up and drop-off” process. Further, using a hBN layer for picking up the stack [6] is currently one of the most effective ways for achieving a clean transfer of the exfoliated layers. Raman spectra of the graphene layer in the assembled van der Waals heterostructure

also showed low signal-to-noise ratio, sharp G and 2D peaks and an absence of D peak, confirming the cleanliness of the transferred graphene flake.

4. **Low-temperature current-induced annealing:** Some of the fabricated devices exhibited low electron mobility, and hence, electron-electron scattering was suppressed by electron-impurity scattering in those devices. To improve the carrier mobility, such devices were subjected to current annealing at low temperatures ($T \sim 20$ K). The devices were annealed to a maximum current of $50 \mu\text{A}$ by increasing in steps of 100 nA . Passing such a large current helps in removing any unwanted dopants from the graphene-hBN interface and other adsorbates, if any [7]. Device D1S2 was subjected to low-temperature current annealing - the transfer characteristics before and after the annealing process are shown in Fig. S2f. The mobility of the device at $T = 10$ K improved from $250,000 \text{ cm}^2\text{V}^{-1}\text{s}^{-1}$ to $650,000 \text{ cm}^2\text{V}^{-1}\text{s}^{-1}$, after the annealing process.

S3. Calculation of the diffusive mean free path in our devices:

Our ultra-clean devices exhibit a range of variation in their n dependence on electrical conductivity σ , i.e. $\sigma \sim n^\alpha$ with $\alpha \in [0.5, 2]$ (Fig. S3a). This variation owes its origin to the

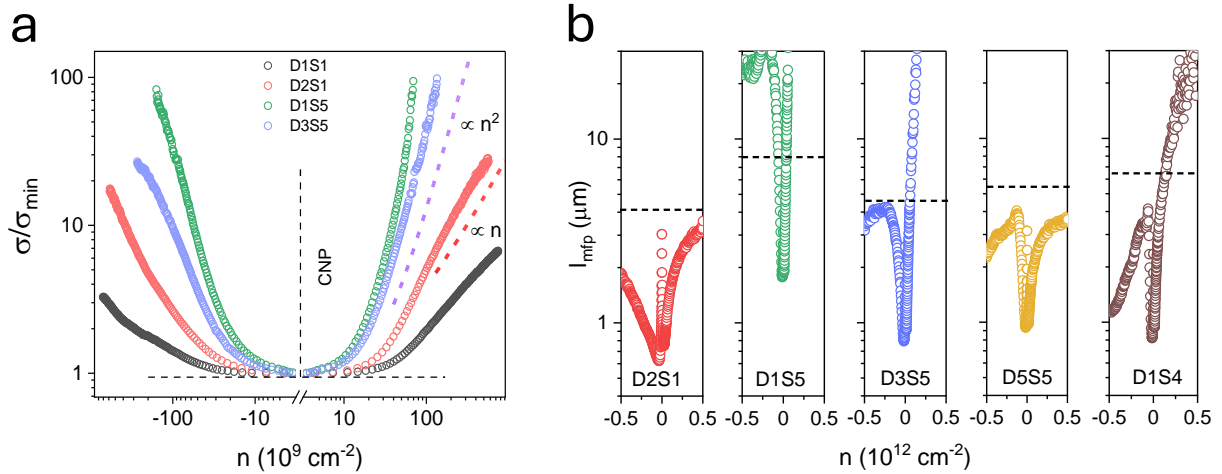


Figure S3. **Mean free path of electrons in hydrodynamic devices:** (a) Normalised electrical conductivity of four devices as a function of n at $T = 110$ K. The red and blue dashed lines serve as guides to the eye. (b) Diffusive mean free path l_{mfp} as a function of n for five devices at $T = 110$ K. The dashed lines indicate the widths of the respective electronic channels.

dominant nature of scattering affecting electrical transport, e.g. $\alpha = 0.5, 1, 2$ respectively indicate ballistic, diffusive and viscous electronic conduction. From the $\sigma - n$ data, we calculate the differential field-effect mobility for the electronic channels in our devices which, as per Drude's model, is given by

$$\mu = \frac{1}{e} \left| \frac{d\sigma}{dn} \right| \quad (1)$$

and the diffusive mean free path (l_{mfp}) which is given by

$$l_{\text{mfp}} = \frac{h\sigma}{2e^2k_{\text{F}}} \quad (2)$$

The diffusive mean free paths for a few of the measured devices, as a function of n , at $T = 110$ K are shown in Fig. S3b. This confirms that $l_{\text{mfp}} \approx W$ for most of our devices and hence, we can easily consider the momentum relaxation length l_{mr} to be equal to the width W of the channel for most of our devices.

S4. Thermal transport measurement circuit:

The thermal transport measurements were carried out using a circuit, whose schematic has been detailed in Fig. S4a. For this measurement, the device was bonded onto a PCB made of FR-4 dielectric, housing an impedance-matching LC tank circuit in coplanar waveguide geometry. The chosen inductor ($L = 220$ nH) and capacitor ($C = 3.9$ pF) result in a resonant frequency of $f_{\text{res}} \simeq \frac{1}{2\pi\sqrt{LC}} \simeq 100$ MHz across the experimental range of temperatures (20 – 300 K). The resonant frequency of the tank circuit was experimentally confirmed using a Keysight E5071C Vector Network Analyser (Fig. S4b and S4c). The impedance-matched RF signal, carrying the thermal noise from the device, was extracted from the cryostat via RG-316 cables and underwent a series of analog and digital processing steps at room temperature. It started with 3 stages of low-noise amplification (ZFL-500LN+ and MITEQ-AU 1291), after which the amplified signal passed through an RF mixer (ZLW-3+), which was fed using a Keysight N5173B signal generator, followed by a low-pass filter (SLP-1.9+) with a cut-off frequency of 1.9 MHz. The resulting signal is then passed through an RF-matched Schottky diode (DMS-104P) which integrates the signal strength over the frequency range and converts the RF power into a DC voltage. The resulting DC voltage, as observed using the Digital Multimeter (Keithley 2002) can be written as

$$V_{\text{dc}} = c \frac{\langle V^2 \rangle}{R} = c \frac{4GLk_{\text{B}}TR\Delta f(1 - \Gamma^2)}{R} = 4cGLk_{\text{B}}T\Delta f(1 - \Gamma^2) \quad (3)$$

Table I. **List of all the measured samples:** Details specifying the channel dimensions, the thickness of the bottom hBN layer, intrinsic charge inhomogeneity, differential field-effect mobility (at $n = 10^{11} \text{ cm}^{-2}$ and $T = 300 \text{ K}$) and diffusive mean free path (at $n = 10^{11} \text{ cm}^{-2}$ and $T = 300 \text{ K}$)

Sample	L (μm)	W (μm)	t_{hBN} (nm)	$n_{\text{min}}(0)$ (10^{10} cm^{-2})	μ ($10^5 \text{ cm}^2/\text{V.s}$)	l_{mfp} (μm)
D1S1	2.2	4.6	22	3.1	0.6	0.5
D2S1	2.1	4.2	22	1.48	2.2	3
D3S1	2.2	4.6	22	1.23	7.3	6
D1S2	1.9	5.2	30	1	0.9	1.12
D1S4	1	6.7	24	0.98	3.74	3.93
D4S4	0.6	0.8	24	1.02	0.2	0.18
D1S5	1.4	8.2	27	0.71	15.4	15.11
D2S5	1	9.1	27	1.78	0.4	0.3
D3S5	1.1	4.6	27	0.84	4.3	3.85
D5S5	1.2	5.7	27	0.92	2.2	1.84
D1S6	1.4	3.4	25	0.99	0.62	0.46
D4S6	1.1	2.4	25	1.1	0.57	0.71
D5S6	1	1.9	25	1.6	0.2	0.16
D1S7	3	10	27	0.69	0.25	0.14
D2S7	3	10	27	0.62	0.2	0.18
D3S7	2.5	10	28	0.99	0.31	0.15

where G is the amplification factor, L is the conversion loss through the mixer and filter, c is the power-to-voltage conversion factor of the diode, Δf is the bandwidth of the measurement, R is the two-terminal resistance of the device under test, $\Gamma^2 = S_{11}$ is the reflectance coefficient and T is the electron temperature. Now, the device under test has a two-terminal resistance (R) has 2 contributions: one from the channel resistance R_{ch} and one from contact resistance R_{c} , and is given by $R = R_{\text{ch}} + 2R_{\text{c}}$. Since R_{ch} is the electrical resistance of interest, Eqn. 3 is modified to

$$V_{\text{dc}} = 4cGLk_{\text{B}}\Delta f(1 - \Gamma^2) \left(\frac{R_{\text{ch}}T_{\text{ch}} + 2R_{\text{c}}T_{\text{c}}}{R_{\text{ch}} + 2R_{\text{c}}} \right) \quad (4)$$

where T_{ch} and T_{c} are respectively the electron temperatures of the channel and the con-

tacts. We further assume a cold phonon bath model for our calculations, which means that heating the channel using a DC bias does not change the temperature of the contacts, significantly [8].

S5. Equations for electron hydrodynamics:

The standard expression for the electrical conductivity in the Drude model is

$$\sigma = \frac{ne^2\tau}{m} \quad (5)$$

where n is the carrier density, τ the relaxation time and m the mass of the carriers as obtained from band structure. Note that the τ , which appears in this expression is the bulk momentum relaxation time. In the hydrodynamic regime of electrical transport, the shear viscosity also contributes to the conductivity rendering the above expression incomplete. Further, for a system like graphene with a linear dispersion, there is no effective mass coming from band

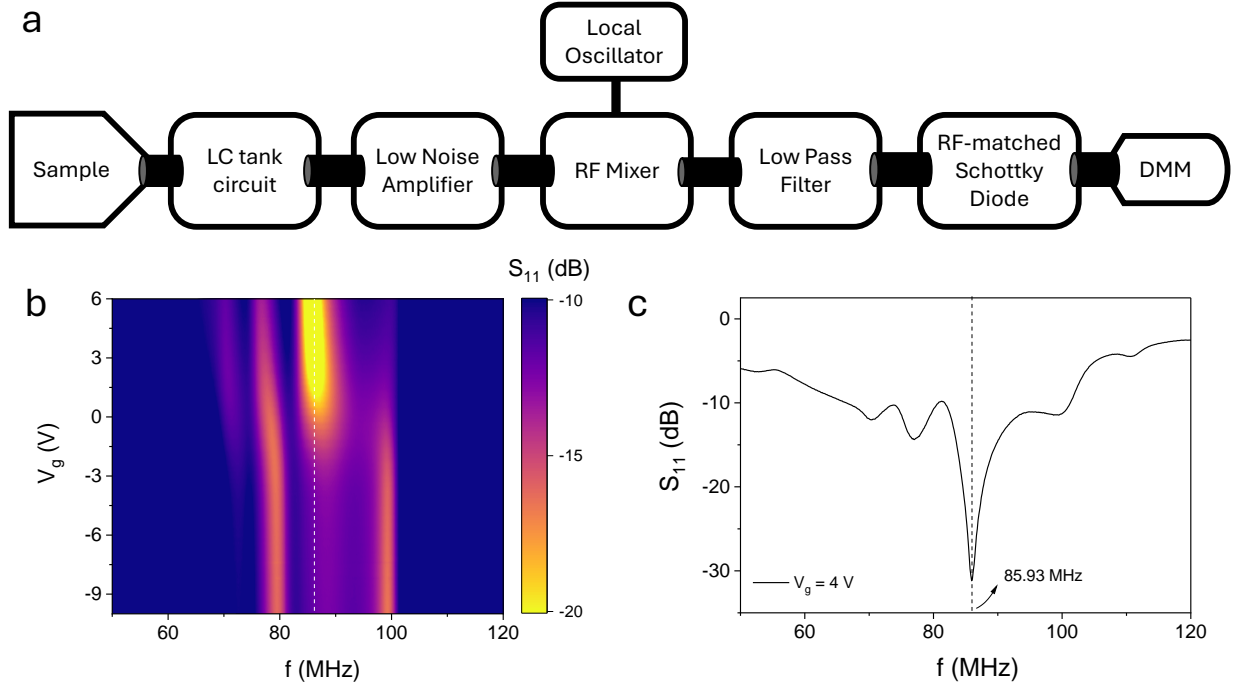


Figure S4. **Measurement of Johnson-Nyquist noise:** (a) Schematic of the circuit for measuring Johnson-Nyquist noise. (b) Colour plot of the reflectance coefficient S_{11} of the device at $T = 20$ K, as a function of signal frequency (f) and applied gate voltage (V_g). (c) S_{11} as a function of f at $V_g = 4$ V.

structure. To incorporate the effects of the shear viscosity and also figure out what replaces the band effective mass in general case, we consider a hydrodynamic description of transport below.

We start with the expression for the stress tensor of a relativistic fluid [9]. The treatment developed below will also be applicable to a non-relativistic fluid but it is most convenient to think of it as the large rest mass limit of a relativistic fluid. The stress tensor is

$$T^{\mu\nu} = p\eta^{\mu\nu} + \frac{(p + \epsilon)}{c^2}U^\mu U^\nu \quad (6)$$

Here p is the pressure of the fluid, ϵ , its energy density including the rest mass energy and $\eta^{\mu\nu}$ is the metric tensor of special relativity. c is the speed of “light”, which we will later set equal to the dispersion velocity of graphene (v_F). For the time being, we will call it c to be consistent with the notation of most papers and books. The relativistic vector \mathbf{U} has the components (U^0, \mathbf{U}) , where the space-like component

$$\mathbf{U} = \frac{\mathbf{v}}{\sqrt{1 - v^2/c^2}} \quad (7)$$

and the time-like component

$$U^0 = \frac{c}{\sqrt{1 - v^2/c^2}} \quad (8)$$

Here \mathbf{v} is the velocity of the fluid. Further, the i^{th} component of the momentum density $\pi_i = T^{0i}/c$. Here i takes on the values 1 and 2 (for a 2D system), which correspond to the x and y directions. We assume that $v \ll c$, which is expected to be true for typical flow velocities in graphene and in this limit, Eqns. 6, 7 and 8 give $\pi_i = (p + \epsilon)v_i$ or in more familiar notation

$$\boldsymbol{\pi} = \frac{(p + \epsilon)}{c^2}\mathbf{v} = \frac{\mathcal{H}}{c^2}\mathbf{v} \quad (9)$$

The quantity $\mathcal{H} = p + \epsilon$ is the enthalpy density (i.e. the enthalpy per unit volume). In the more familiar case of a non-relativistic fluid

$$\boldsymbol{\pi} = \rho\mathbf{v} \quad (10)$$

where ρ is the density of the fluid. Thus, more generally \mathcal{H}/c^2 acts as the mass density of a fluid. In particular for the case of the non-relativistic fluid (i.e. a fluid in which the

rest mass energy of the particles is much higher than any other energy scale), $\mathcal{H}/c^2 \approx \rho$ and we get Eqn. 10. We will see below that \mathcal{H}/c^2 replaces ρ in all the usual expressions we encounter in the context of transport.

Having obtained the appropriate expression for $\boldsymbol{\pi}$, let us now focus on the Navier-Stokes equation for the fluid. In particular, we are interested in steady-state laminar (low Reynolds number) flow solutions due to an applied electric field \mathbf{E} . The relevant equation for this is

$$-\eta \nabla^2 \mathbf{v} = ne\mathbf{E} \quad (11)$$

where η is the shear viscosity of the fluid and n its number density. The above equation is for the flow of a fluid with strict momentum conservation in the bulk. In the presence of momentum relaxation in the bulk, the equation becomes

$$\begin{aligned} -\eta \nabla^2 \mathbf{v} &= ne\mathbf{E} - \frac{\boldsymbol{\pi}}{\tau} \\ &= ne\mathbf{E} - \frac{\mathcal{H}\mathbf{v}}{v_F^2 \tau} \end{aligned} \quad (12)$$

Here, τ is the bulk momentum relaxation time and v_F is the Fermi velocity of graphene.

S6. Electrical conductivity of hydrodynamic electrons:

We now focus on a geometry in 2D in which the flow is along the x direction in a channel of width W . Eqn. 12 can be solved in this geometry with no-slip conditions at the channel edges. The solution is

$$v_x(y) = -\frac{env_F^2 \tau}{\mathcal{H}} \left[1 - \frac{\cosh\left(\sqrt{\frac{\mathcal{H}}{v_F^2 \eta \tau}} y\right)}{\cosh\left(\sqrt{\frac{\mathcal{H}}{v_F^2 \eta \tau}} \frac{W}{2}\right)} \right] E \quad (13)$$

with $y = 0$ at the centre of the channel. The total current

$$I = -en \int_{-W/2}^{W/2} v_x(y) dy \quad (14)$$

$$= \frac{e^2 n^2 v_F^2 \tau}{\mathcal{H}} \left[W - 2\sqrt{\frac{v_F^2 \eta \tau}{\mathcal{H}}} \tanh\left(\sqrt{\frac{\mathcal{H}}{v_F^2 \eta \tau}} \frac{W}{2}\right) \right] E \quad (15)$$

The conductivity is thus

$$\sigma = \frac{e^2 n^2 v_F^2 \tau}{\mathcal{H}} \left[1 - \frac{\tanh\left(\sqrt{\frac{\mathcal{H}}{v_F^2 \eta \tau}} \frac{W}{2}\right)}{\sqrt{\frac{\mathcal{H}}{v_F^2 \eta \tau}} \frac{W}{2}} \right] \quad (16)$$

In the limit in which there is perfect momentum relaxation in the bulk (i.e. $\tau \rightarrow \infty$), Eqn. 16 reduces to

$$\sigma = \frac{e^2 n^2 W^2}{12\eta} \quad (17)$$

In the other limit, in which there is no effect of the shear viscosity (i.e. $\eta \rightarrow 0$),

$$\sigma = \frac{e^2 n^2 v_F^2 \tau}{\mathcal{H}} \quad (18)$$

which is just the usual expression obtained from the Drude model with the quantity $\mathcal{H}/(v_F^2 n)$ playing the role of the mass of the charge carrier. From the forms of Eqns. 16 and 17, we can define an effective shear viscosity η_{eff} when both the effects of viscosity and momentum relaxation are present, which is

$$\eta_{eff} = \frac{W^2 \mathcal{H}}{12v_F^2 \tau} \left[1 - \frac{\tanh\left(\sqrt{\frac{\mathcal{H}}{v_F^2 \eta \tau}} \frac{W}{2}\right)}{\sqrt{\frac{\mathcal{H}}{v_F^2 \eta \tau}} \frac{W}{2}} \right]^{-1} \quad (19)$$

so that the conductivity

$$\sigma = \frac{e^2 n^2 W^2}{12\eta_{eff}} \quad (20)$$

In the limit $\tau \rightarrow \infty$, $\eta_{eff} = \eta$ as expected whereas in the opposite limit $\eta \rightarrow 0$,

$$\eta_{eff} = \frac{W^2 \mathcal{H}}{12v_F^2 \tau} \quad (21)$$

to yield Eqn. 18. Note that the conductivity obtained from all four Eqns. 16, 17, 18 and 20 goes to zero as n goes to zero. While this seems intuitively obvious (there should be no transport if there are no carriers), it is not quite correct in the case of a system like graphene with particle-hole symmetry and a charge neutrality point (CNP). When the chemical potential is at the CNP, the net carrier density is indeed zero. However, electrons and holes (which are of equal density and hence combine to give $n = 0$) can individually have non-zero densities. Each species can thus carry a current which can be degraded giving rise to an electrical conductivity σ_{min} at the CNP even when $n = 0$. The total conductivity is thus the sum of σ_{min} and the expression obtained from Eqn. 16 (or equivalently Eqn. 20),

$$\sigma = \sigma_{min} + \frac{e^2 n^2 W^2}{12\eta_{eff}} \quad (22)$$

and in the limit $\eta \rightarrow 0$, this becomes

$$\sigma = \sigma_{\min} + \frac{e^2 n^2 v_F l_m}{\mathcal{H}} \quad (23)$$

with the momentum relaxation length $l_m = v_F \tau$, which is the expression that has been used to obtain \mathcal{H} assuming that $l_m = W$ (which is the condition for Knudsen flow). Note that the above expression is obtained only in the limit $\eta \rightarrow 0$ or more correctly,

$$\eta \ll \frac{W^2 \mathcal{H}}{4 v_F l_m} \quad (24)$$

S7. Violation of Wiedemann-Franz Law in lower mobility devices:

The violation of the WF law in disordered monolayer graphene may not necessarily imply the existence of a hydrodynamic Dirac fluid near the charge neutrality point. Violations originating due to the presence of disorder [10, 11], band gap opening at the Dirac point [12], bipolar diffusion [13], etc. have similar orders of magnitude as those observed in the low-mobility graphene devices considered here. As a result, the origin of the WF violation in these devices needs to be understood properly. Among the devices listed in Table 1, D1S1 is the most disordered, with $n_{\min}(0) \approx 3 \times 10^{10} \text{ cm}^{-2}$ and a detailed study of this device is expected to provide valuable information to resolve the origin of WF violation in these disordered graphene systems.

To understand the role of electron-impurity scattering in this scenario, we construct a phenomenological model based on a combination of short- and long-range impurity scattering processes. Short-range scattering is independent of the electronic energy (ϵ) and mainly includes neutral defects with a delta function potential. In contrast, long-ranged impurity scattering involves the Coulombic interaction between electrons and charged impurities. The resulting relaxation time for such a combination of scattering processes follows the Matthiessen rule and is given by (up to some overall constant):

$$\tau^{-1}(\epsilon) = \gamma |\epsilon| + \frac{1 - \gamma}{|\epsilon|} \quad (25)$$

Here, $\gamma = 1$ corresponds to purely short-range (and acoustic phonon) scattering and $\gamma = 0$ corresponds to purely long-range scattering. Although γ usually exhibits a non-trivial temperature dependence, this can be ignored for studying the qualitative behaviour of \mathcal{L} .

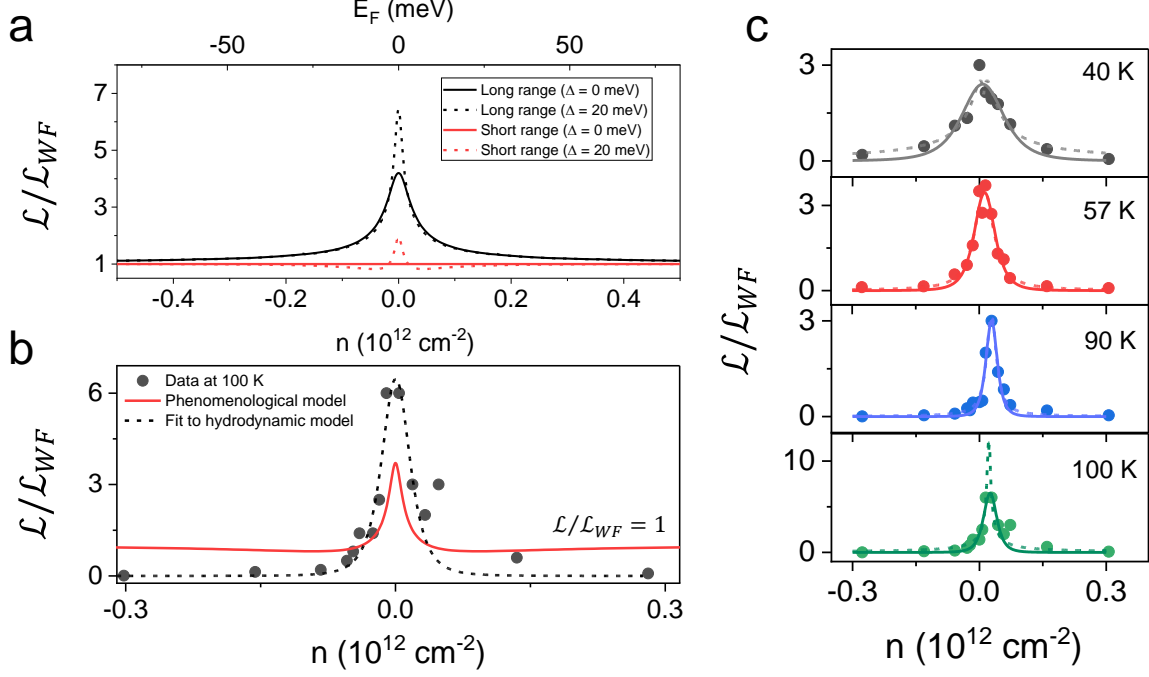


Figure S5. **Fitting the experimental data to a Dirac fluid model and a phenomenological diffusive scattering-based model:** (a) Theoretically calculated $\mathcal{L}/\mathcal{L}_{WF}$ vs n for long-range and short-range interactions, both in the presence ($\Delta = 20 \text{ meV}$) and absence ($\Delta = 0$) of a small band gap at the Dirac point. (b) Comparison of the experimental $\mathcal{L}/\mathcal{L}_{WF}$ vs n data for D1S1 at 100 K with theoretical predictions of the phenomenological model Eqn. 25 and the hydrodynamic model Eqn. 30. (c) $\mathcal{L}/\mathcal{L}_{WF}$ vs n for D1S1 at different temperatures. The solid circles represent the experimental data points, the solid line represents the fit as per the hydrodynamic model Eqn. 29, and the dashed line represents the fit as per the linear-density corrected model Eqn. 30. The R^2 values for the fits of Eqn. 29 to the data, respectively, vary between 90 – 95 %.

Within the relaxation-time approximation, the electrical and thermal conductivities are given by:

$$\sigma = e^2 \int d\epsilon \left(-\frac{\partial f^0}{\partial \epsilon} \right) g(\epsilon) v^2(\epsilon) \tau(\epsilon) \quad (26)$$

$$\kappa = \frac{1}{T} \int d\epsilon (\epsilon - \mu)^2 \left(-\frac{\partial f^0}{\partial \epsilon} \right) g(\epsilon) v^2(\epsilon) \tau(\epsilon) \quad (27)$$

where $g(\epsilon)$ is the electronic density of states, $\mu = E_F$ is the chemical potential, $v(\epsilon)$ is the dispersion velocity, and $f^0(\epsilon)$ is the equilibrium distribution function. By using the graphene dispersion relation $\epsilon = \hbar v k$, we get the respective transport coefficients, which, in turn, yield the Lorentz number \mathcal{L} for different carrier densities. Fig. S5a shows the variation of $\mathcal{L}/\mathcal{L}_{WF}$ as

a function of n for different combinations of scattering mechanisms. In the presence of purely short-ranged scattering processes, the Wiedemann-Franz law remains valid for all values of n since the scattering process is independent of the electronic energy. On the other hand, long-ranged Coulomb scattering results in an enhancement of $\mathcal{L}/\mathcal{L}_{\text{WF}}$ above 1 near the Dirac Point. However, the saturation of $\mathcal{L}/\mathcal{L}_{\text{WF}}$ to 1 at large n owes its origin to the dominant contribution from short-ranged scattering for $\epsilon \gg \epsilon_c = \sqrt{\frac{1-\gamma}{\gamma}}$ in Eqn. (25). Thus, for $\mu > \epsilon_c$, the integrals in Eqn. (26) and Eqn. (27) are approximately the same as the coefficients in the presence of short-ranged scattering, restoring the Lorentz ratio to the value dictated by the Wiedemann-Franz law. In addition to impurity scattering events contributing to WF violation, we also note that in graphene-based vdW heterostructures, the presence of defects and interfacial disorder [14] as well as strain caused by the encapsulating hBN substrate [15] can open up a gap at the Dirac point. This band gap [12] can be responsible for a non-trivial variation of $\mathcal{L}/\mathcal{L}_{\text{WF}}$ with n , usually characterised by an enhancement at low densities. The experimentally obtained band gap for device D1S1 is $\simeq 23$ meV, which has also been used for the theoretical calculation of $\mathcal{L}/\mathcal{L}_{\text{WF}}$ in Fig. S5a, assuming the simple model proposed in [12], where the density of states $g(\epsilon)$ for the conduction (+) and valence (-) band is given by the same linear spectrum now displaced by the gap Δ .

$$g_{\pm}(\epsilon) = \frac{2}{\pi \hbar v_F^2} |\epsilon \mp \Delta/2| \quad (28)$$

As a function of carrier density, $\mathcal{L}/\mathcal{L}_{\text{WF}}$ for D1S1 exhibits a range of values similar to what is expected from a combination of short- and long-range scattering mechanisms. However, certain features in the data cannot be explained by the above-mentioned mechanisms, as can be observed in Fig. S5b. Firstly, any combination of short- and long-range scattering processes leads to a simultaneous enhancement and suppression of $\mathcal{L}/\mathcal{L}_{\text{WF}}$ as a function of n with the dip reaching a minimum value of $\sim 0.8 \mathcal{L}_{\text{WF}}$, but the experimental data for D1S1 shows that \mathcal{L} can be as low as $0.01 \mathcal{L}_{\text{WF}}$ at high densities. Secondly, the experimental $\mathcal{L}/\mathcal{L}_{\text{WF}}$ for D1S1 does not saturate to 1 for higher values of n ($\gtrsim 10^{15} \text{ m}^{-2}$). Such saturation was observed in the behaviour of \mathcal{L} in Ref. [16] and the authors attributed it to the absence of hydrodynamic electrons at high densities. Both these factors point towards the incompatibility of our phenomenological model in explaining the experimental data for D1S1, which is further exemplified by the quality of fit in Fig. S5b. Lastly, opening up a band gap at the Dirac point can partially account for the enhancement of $\mathcal{L}/\mathcal{L}_{\text{WF}}$ near $n = 0$ but this

mechanism does not allow for any suppression of $\mathcal{L}/\mathcal{L}_{\text{WF}}$ below 1. Hence, this mechanism also is not the right choice for the origin behind the WF violation in D1S1.

We also believe that bipolar diffusion (BD) of electrons and holes does not play a significant role in the observed non-trivial variation of $\mathcal{L}/\mathcal{L}_{\text{WF}}$ for D1S1. Previous reports [12, 16] show that in the presence of BD, there is an additional contribution to the electronic thermal conductivity, thereby resulting in an enhancement of $\mathcal{L}/\mathcal{L}_{\text{WF}}$. However, this mechanism does not provide any avenue for a possible suppression of $\mathcal{L}/\mathcal{L}_{\text{WF}}$ below 1 at high densities.

Finally, we fit the observed variation of $\mathcal{L}/\mathcal{L}_{\text{WF}}$ as a function of n at different temperatures, for device D1S1, to Eqn. 3 from the main text, given by:

$$\mathcal{L}/\mathcal{L}_{\text{WF}} = \frac{a}{\left[1 + \left(\frac{n}{b}\right)^2\right]^2} \quad (29)$$

where a and b are fitting parameters. The fit is shown in Figs. S5b and S5c. We obtain a significantly high coefficient of determination (R^2), indicating the presence of electron hydrodynamics rather than diffusive scattering even in D1S1. We further observe a consistent underfitting of the observed data for higher densities, indicating the presence of finite density corrections to the terms evaluated at the critical point. Motivated by the conductivity becoming linear for large n , we introduce a linear finite density correction to the enthalpy density, giving the new fit as:

$$\mathcal{L}/\mathcal{L}_{\text{WF}} = \frac{a(1 + c|n|)}{\left[1 + \frac{\left(\frac{n}{b}\right)^2}{1 + c|n|}\right]^2} \quad (30)$$

where c is an additional fitting parameter. The inclusion of this additional parameter improves the fit at large densities, as shown by the dashed curves in Fig. S5c for different temperatures. Thus, we expect D1S1 to remain in the hydrodynamic regime, albeit deviate away from quantum criticality as we stray further away from the charge neutrality point.

S8. Quantum critical conductivity for hydrodynamic electrons:

The expression for the electronic thermal conductivity κ_e from the general theory of critical hydrodynamic transport can be obtained as follows. The expression for the electrical conductivity at zero frequency and zero magnetic field is [17]

$$\sigma = \sigma_Q \tau_{\text{mr}} (\psi + 1/\tau_{\text{mr}}) \quad (31)$$

where

$$\psi = \frac{4e^2 \rho^2 v_F^2}{\sigma_Q \mathcal{H}}$$

and τ_{mr} is the momentum relaxation time, ρ , the density of carriers, v_F , the Fermi velocity and \mathcal{H} is the enthalpy density. The quantum of conductance

$$\sigma_Q = \Phi_\sigma \frac{4e^2}{h} \quad (32)$$

where Φ_σ is a universal dimensionless number that depends only on the universality class of the critical point. The electronic thermal conductivity at zero frequency and zero magnetic field is given by the expression [17]

$$\kappa_e = \frac{1}{\Phi_\sigma} \frac{h}{4e^2} \frac{\mathcal{H} \sigma_Q v_F^2}{\psi + 1/\tau_{mr}} \quad (33)$$

Combining Eqns. 31, 32 and 33, we get

$$\kappa_e = \frac{\sigma_Q \mathcal{H} v_F l_{mr}}{T \sigma} \quad (34)$$

which is Eqn. 2 of the main text. Here the momentum relaxation length $l_{mr} = v_F \tau_{mr}$.

S9. Relation between the shear viscosity and enthalpy density:

Within standard kinetic theory, the shear viscosity of a non-relativistic 2D fluid is

$$\eta = \frac{1}{2} n m \bar{v} l \quad (35)$$

where n is the density, m , the mass of the fluid particles, \bar{v} , their mean speed and l , the mean free path for collision among the fluid particles. For a relativistic fluid, this becomes

$$\eta = \frac{\mathcal{H} l}{2 v_F} \quad (36)$$

where we have substituted \mathcal{H}/v_F^2 for the mass density nm as per the argument after Eqn. 10 and also set $\bar{v} = v_F$. Thus, \mathcal{H} obtained from the experimental measurements using Eqn. 23 can be substituted in Eqn. 36 to obtain η provided l is known and the consistency condition 24 is satisfied. In fact the consistency condition can be checked after η has been obtained this way. Using Eqn. 36, the consistency condition can also be written as

$$W \gg \sqrt{2 l l_m} \quad (37)$$

which only involves the three relevant length scales W , l_m and l . Further if $l_m = W$, the condition simply becomes $W \gg 2l$. The important quantity here is thus l , which, for the electron fluid, becomes the momentum-conserving electron-electron scattering length. For a Dirac fluid of electrons (i.e. when the Fermi energy is “very close” to the CNP), this has been argued to be of the form,

$$l \sim \frac{\hbar v_F}{\alpha^2 k_B T} \quad (38)$$

where $\alpha = e^2/(\hbar v_F)$ is the “effective” fine structure constant. Substituting, Eqn. 38 in Eqn. 36, we get

$$\eta \sim \frac{\mathcal{H} \hbar}{\alpha^2 k_B T} \quad (39)$$

Let us now consider the enthalpy density

$$\mathcal{H} = \epsilon + p = \mu n + T s \quad (40)$$

from the Gibbs-Duhem relation, where μ is the chemical potential and s , the entropy density. At the CNP, $\mu = 0$, $n = 0$ and thus, $\mathcal{H} = T s$ at all temperatures. Further $s \sim k_B \left(\frac{k_B T}{\hbar v_F} \right)^2$, which implies that

$$\mathcal{H} = \frac{(k_B T)^3}{\hbar^2 v_F^2} \quad (41)$$

substituting which into Eqn. 39, we find that

$$\eta \sim (k_B T)^2 \frac{\hbar}{e^4} \quad (42)$$

at the CNP. Note that v_F does not appear in this expression, which is fortuitous since v_F gets renormalised to infinity at the CNP.

S10. Thermal modelling of the hBN-encapsulated graphene devices:

The flow of Joule heat within the device can be understood using a simple toy model. To achieve thermal equilibrium, the hot electrons in graphene can undergo thermal relaxation via four different processes -

- out-diffusion through the metallic electrodes,
- interaction with the graphene phonons,

- conduction through the adjacent hBN layers, and
- radiative infrared emission into the environment

Using the heat diffusion equation, this can be expressed as

$$\dot{Q}(\vec{r}) = -\vec{\nabla} \cdot \left[\kappa_e \vec{\nabla} T_e(\vec{r}) \right] + A \Sigma \left[T_e^4(\vec{r}) - T_{\text{ph}}^4 \right] + P_{\text{substrate}} + P_{\text{rad}} \quad (43)$$

where Q is the thermal charge injected into the channel due to Joule heating, κ_e is the thermal conductivity, $T_e(\vec{r})$ is the electron temperature at any point denoted by \vec{r} , T_{ph} is the lattice temperature, A is the sample area, Σ is the electron-phonon coupling constant, $P_{\text{substrate}}$ is the thermal power lost to the substrate and P_{rad} is the radiated thermal power density.

Now, the thermal energy leaking into the electromagnetic environment [18] formed by the electrical measurement system via the emission and absorption of blackbody photons is given by the thermal radiative conductance, $G_{\text{rad}} = \frac{\pi^2 k_B B}{3}$ where B is the bandwidth of measurement. Usually for a measurement bandwidth of 4 MHz, $G_{\text{rad}} \sim 10^{-15}$ W/K and hence, G_{rad} and subsequently, P_{rad} can be neglected in Eqn. 43.

Further, due to the weak electron-phonon coupling of graphene [3], the heat dissipated by the electronic subsystem to the lattice is quite small and, for $|T_e - T_{\text{ph}}| \ll T_{\text{ph}}$, the thermal conductance of the electron-phonon channel is reduced to $G_{\text{ep}} = 4A\Sigma T_{\text{ph}}^3$, which can also be neglected in comparison to the heat reaching the metallic electrodes.

In addition to this, the hBN substrate used in our experiment has a much larger surface optical phonon energy (102 meV) and hence can influence the electron cooling process at high T_e but can be neglected in this case since experimentally T_e never exceeds 700 K [19]. Also the hyperbolic phonon-polariton modes of hBN, responsible for dissipating heat away from the graphene electrons, have two Reststrahlen bands around 100 meV [20], which indicates that these modes also do not take away heat from the graphene channel under the experimental conditions described in our paper. Hence, we can conclude that heat leakage through the hBN substrate ($P_{\text{substrate}}$) can also be neglected.

Further, assuming heat flow predominantly only along the direction of current flow, we can rewrite Eqn. 43 as the 1D Fourier's equation

$$q = -\kappa_e \nabla T_e(x) \quad (44)$$

where q is the rate of heat flow into the channel and $T_e(x)$ is the electron temperature at any point x along the direction of current flow.

Under thermal equilibrium, the total heat injected into the graphene channel is given by

$$q = JWE L \quad (45)$$

Further, as per Wiedemann Franz Law, we also have

$$\kappa_e = \mathcal{L} \sigma T_e(x) \frac{dT_e(x)}{dx} W \quad (46)$$

This leads to the following equality:

$$\frac{1}{2} \frac{d}{dx} [T_e^2(x)] = E^2 \frac{L}{\mathcal{L}} \quad (47)$$

Since the metallic electrodes have a much higher thermal conductivity, they can be considered to have the same temperature T_c despite the Joule heating in the channel. Hence, $T_e(x=0) = T_e(x=L) = T_c$ and the temperature profile is symmetric about $x = \frac{L}{2}$.

Thus, Eqn. 47 gives

$$\int_{T_c}^{T_e(x)} d(T_e^2(x)) = \frac{2L}{\mathcal{L}} E^2 \int_0^x dx \Rightarrow T_e^2(x) - T_c^2 = \frac{2L}{\mathcal{L}} E^2 f(x) \quad (48)$$

where $f(x) = x$ when $x \in [0, L/2]$ and $f(x) = L - x$ when $x \in [L/2, L]$.

This leads to a temperature profile which can be written as:

$$T_e(x) = \begin{cases} \sqrt{T_c^2 + \frac{2L}{\mathcal{L}} E^2 x} & \text{for } 0 \leq x \leq L/2 \\ \sqrt{T_c^2 + \frac{2L}{\mathcal{L}} E^2 (L - x)} & \text{for } L/2 \leq x \leq L \end{cases}$$

The thermal profile peaks at $x = L/2$, where the maximum temperature is given by

$$T_e^{\max}(x) = T_e(x = L/2) = \sqrt{T_c^2 + \frac{L^2 E^2}{\mathcal{L}}} \quad (49)$$

The measured thermal noise gives a non-weighted spatial average of the electronic temperature (T_e) along the channel length.

$$T_e = \langle T_e(x) \rangle = \frac{1}{L} \int_0^L T_e(x) dx \quad (50)$$

Solving the integral, we get

$$T_e = \frac{2\mathcal{L}}{3L^2E^2} \left[\left(T_c^2 + \frac{L^2}{\mathcal{L}} E^2 \right)^{3/2} - (T_c^2)^{3/2} \right] \quad (51)$$

-
- [1] C. R. Dean, A. F. Young, I. Meric, C. Lee, L. Wang, S. Sorgenfrei, K. Watanabe, T. Taniguchi, P. Kim, K. L. Shepard, *et al.*, Boron nitride substrates for high-quality graphene electronics, *Nat. Nanotechnol.* **5**, 722 (2010).
 - [2] W. Wang, X. Ma, Z. Dai, S. Zhang, Y. Hou, G. Wang, Q. Li, Z. Zhang, Y. Wei, and L. Liu, Mechanical behavior of blisters spontaneously formed by multilayer 2D materials, *Adv. Mater. Int.* **9**, 2101939 (2022).
 - [3] A. C. Ferrari, J. C. Meyer, V. Scardaci, C. Casiraghi, M. Lazzeri, F. Mauri, S. Piscanec, D. Jiang, K. S. Novoselov, S. Roth, *et al.*, Raman spectrum of graphene and graphene layers, *Phys. Rev. Lett.* **97**, 187401 (2006).
 - [4] Y.-C. Lin, C. Jin, J.-C. Lee, S.-F. Jen, K. Suenaga, and P.-W. Chiu, Clean transfer of graphene for isolation and suspension, *ACS Nano* **5**, 2362 (2011).
 - [5] J. Yan, Y. Zhang, P. Kim, and A. Pinczuk, Electric field effect tuning of electron-phonon coupling in graphene, *Phys. Rev. Lett.* **98**, 166802 (2007).
 - [6] L. Wang, I. Meric, P. Huang, Q. Gao, Y. Gao, H. Tran, T. Taniguchi, K. Watanabe, L. Campos, D. Muller, *et al.*, One-dimensional electrical contact to a two-dimensional material, *Science* **342**, 614 (2013).
 - [7] J. Moser, A. Barreiro, and A. Bachtold, Current-induced cleaning of graphene, *Appl. Phys. Lett.* **91** (2007).
 - [8] M. L. Roukes, M. Freeman, R. Germain, R. Richardson, and M. Ketchen, Hot electrons and energy transport in metals at millikelvin temperatures, *Phys. Rev. Lett.* **55**, 422 (1985).
 - [9] S. Weinberg, *Gravitation and Cosmology: Principles and Applications of the General Theory of Relativity* (Wiley, 1972).
 - [10] R. Raimondi, G. Savona, P. Schwab, and T. Lück, Electronic thermal conductivity of disordered metals, *Phys. Rev. B - Cond. Matt. and Mat. Phys.* **70**, 155109 (2004).
 - [11] K. Michaeli and A. M. Finkel'stein, Quantum kinetic approach for studying thermal transport

- in the presence of electron-electron interactions and disorder, Phys. Rev. B - Cond. Matt. and Mat. Phys. **80**, 115111 (2009).
- [12] Y.-T. Tu and S. D. Sarma, Wiedemann-Franz law in graphene, Phys. Rev. B **107**, 085401 (2023).
 - [13] H. Yoshino and K. Murata, Significant enhancement of electronic thermal conductivity of two-dimensional zero-gap systems by bipolar-diffusion effect, Journ. of the Phys. Soc. of Jap. **84**, 024601 (2015).
 - [14] M. Evaldsson, I. V. Zozoulenko, H. Xu, and T. Heinzl, Edge-disorder-induced Anderson localization and conduction gap in graphene nanoribbons, Phys. Rev. B - Cond. Matt. and Mat. Phys. **78**, 161407 (2008).
 - [15] J. Jung, A. M. Da Silva, A. H. MacDonald, and S. Adam, Origin of band gaps in graphene on hexagonal boron nitride, Nat. Commun. **6**, 6308 (2015).
 - [16] J. Crossno, J. K. Shi, K. Wang, X. Liu, A. Harzheim, A. Lucas, S. Sachdev, P. Kim, T. Taniguchi, K. Watanabe, *et al.*, Observation of the Dirac fluid and the breakdown of the Wiedemann-Franz law in graphene, Science **351**, 1058 (2016).
 - [17] S. A. Hartnoll, P. K. Kovtun, M. Müller, and S. Sachdev, Theory of the Nernst effect near quantum phase transitions in condensed matter and in dyonic black holes, Phys. Rev. B **76**, 144502 (2007).
 - [18] J. B. Pendry, Quantum limits to the flow of information and entropy, Jour. of Phys. A: Math. and Gen. **16**, 2161 (1983).
 - [19] A. Betz, S. H. Jhang, E. Pallecchi, R. Ferreira, G. Fève, J.-M. Berroir, and B. Plaçais, Super-collision cooling in undoped graphene, Nat. Phys. **9**, 109 (2013).
 - [20] K.-J. Tielrooij, N. C. Hesp, A. Principi, M. B. Lundeberg, E. A. Pogna, L. Banszerus, Z. Mics, M. Massicotte, P. Schmidt, D. Davydovskaya, *et al.*, Out-of-plane heat transfer in van der waals stacks through electron-hyperbolic phonon coupling, Nat. Nanotechnol. **13**, 41 (2018).